An elliptic foil rotating in uniform low-Reynolds number flows

Ruifeng Hu[1]‡ **and Hui Tang**[2]

[1]Key Laboratory of Mechanics on Disaster and Environment in Western China, Ministry of Education, and Department of Mechanics and Engineering Sciences, College of Civil Engineering and Mechanics, Lanzhou University, Lanzhou, China
[2]Department of Mechanical Engineering, Hong Kong Polytechnic University, Kowloon, Hong Kong, China

E-mail: hurf@lzu.edu.cn

Abstract. A computational study is conducted to systematically investigate the effect of rotating speed on vortex shedding characteristics and far-field wake patterns of an elliptic foil rotating in uniform cross flows at low Reynolds numbers. It is found that at low rotating speed, vortices shed at the advancing and retreating edges of the foil could form a strong vortex pair in the wake. At high rotating speed, adjacent vortices are closer to each other, thus may evolve into a single vortex. The far-field wake pattern also strongly depends on the rotating speed and demonstrates complex behaviors. It is observed that the wake can defect from downwards to upwards by increasing the rotating speed. The mean lift force increases monotonically with the rotating speed, while a significant drag reduction occurs at a small rotating speed, which is explained by the corresponding wake pattern. Furthermore, there exists a rotating speed regime in which the mean aerodynamic torque is positive so that the rotation of the foil could be solely promoted by the flow, indicating a possibility of flow energy harvesting in this regime.

Keywords: rotating foil, vortex shedding, far-field wake, wake deflection

‡ Corresponding author: hurf@lzu.edu.cn

1. Introduction

Object's rotating in a flow is a very common phenomenon in nature and engineering applications, such as rotary wings, wind turbines, windmills, water wheels, etc. Generally, rotating motion can be classified into two types based on the rotation axis with respect to the flow direction, namely the parallel-axis and the vertical-axis rotations (Lugt, 1983), the latter being the main focus of this paper. Examples of the vertical-axis rotation include Savonius-type wind turbine (Akwa et al., 2012; Roy and Saha, 2013), vortex-induced autorotating wing or cylinder with the axis perpendicular to the freestream (Smith, 1971; Iversen, 1979; Lugt, 1980; Skews, 1990; Wang et al., 2011; Greenwell and Garcia, 2014; Hargreaves et al., 2014; Ryu and Iaccarino, 2017), windborne plate-like debris flying in tumbling mode (Tachikawa, 1983; Lin et al., 2006; Kakimpa et al., 2012; Uchibori and Tamura, 2019) and tumbling motion of a thin plate in free fall (Belmonte et al., 1998; Andersen et al., 2005; Tam et al., 2010; Wang et al., 2013; Hu and Wang, 2014; Lau et al., 2018), among many others.

To the authors' knowledge, Lugt and Ohring (1977) performed the first computational investigation on an elliptic foil rotating in a uniform flow with a constant spinning rate. In their study, the Reynolds number $Re = U_\infty c/\nu$ (where U_∞ is the freestream velocity, c is the chord length of the foil and ν is the kinematic viscosity of the fluid) is 200, and the non-dimensional rotating speed ω^* ($\omega^* = \omega c/2U_\infty$, where ω is the rotating speed of the foil) is set to 0.5 and 2.0. At $\omega^* = 0.5$, a pair of two counter-rotating vortices was observed to be shed from the advancing and retreating edges of the foil during each half rotation, and the aerodynamic coefficients exhibited periodic variations. Irregular vortex shedding pattern and aerodynamic performance were observed for the $\omega^* = 2.0$ case. The first experimental measurement was carried out by Lua et al. (2010). In their study, two-dimensional flow field around a rotating elliptic foil was obtained by digital particle image velocimetry (DPIV) technique. The non-dimensional rotating speed ω^* was chosen to be 0.417, 0.833, 1.667 and 2.5, and the Reynolds number Re is set to 200 and 1000. At lower rotating speeds ($\omega^* < 1.0$), they observed similar flow characteristics with the $\omega^* = 0.5$ case of Lugt and Ohring (1977). While at high rotating speed ($\omega^* > 1.0$), they observed that adjacent vortices may merge together to form a new "hovering vortex", staying at the top of the foil for several periods, for the first time. In a recent work, Hu (2015) computed three-dimensional flow structures around a rotating wing of elliptic cross section with finite span, under the conditions of the non-dimensional rotating speed ω^* =0.417, 0.833 and 1.667, Reynolds number $Re = 200$, and aspect ratio AR =2, 4 and 6. Here $AR = w/c$, and w is the wing span. It was confirmed that there exists periodic vortex shedding pattern (vortex rings in three dimension) at low rotating speeds, while vortices may cluster near the wing when rotating speed is high enough. Naik et al. (2017) performed a computational study for the effect of thickness ratio (ratio between major and minor axis of an elliptic cylinder) on the vortex shedding and aerodynamics of a rotating elliptic cylinder. They found lift decreases monotonically, but drag decreases first and then increases with

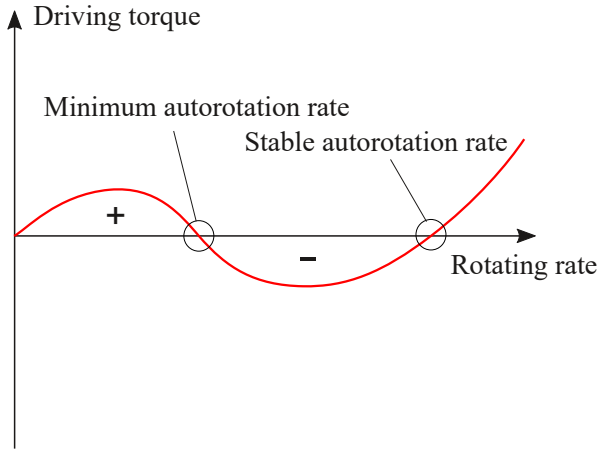

Figure 1. The "Riabouchinsky curve" for the autorotation phenomenon (Lugt, 1983).

thickness ratio. Lua et al. (2018) also carried out numerical simulation to study the thickness ratio effect, but reached a much higher rotating speed of $\omega^* = 2.5$, at which the vortex shedding of a rotating circular cylinder disappears. They also found the decreasing-increasing trend of drag force with thickness ratio. More interestingly, the minimum drag at $\omega^* = 2.5$ is negative, indicating that a thrust is generated. Lu et al. (2018) extended the rotating speed to much higher values ($3.0 < \omega^* < 5.0$), reporting various wake patterns and aerodynamic performances in this regime.

The phenomenon of autorotation is a special equilibrium rotating state at which the aerodynamic torque (also the external driving torque) is zero. Lugt (1983) presented a thorough overview on this topic more than 30 years ago. The mechanism of autorotation can be generally explained by the "Riabouchinsky curve", as illustrated in figure 1, in which the driving torque required to sustain an object's rotation is plotted against the rotating speed. There are three equilibrium points in the curve at which the external torque is zero. Except for $\omega = 0$, the other two non-zero equilibrium points are illustrated in figure 1, and the equilibrium point with larger rotating rate can be referred to the stable rotation with $dM_d/d\omega > 0$ (M_d is the driving torque). In recent years, renewed interests on the autorotating phenomenon is arising due to its potential applications in engineering. Greenwell and Garcia (2014) re-analyzed previous published data and performed new wind-tunnel test to improve the empirical formulations for the autorotating properties. Hargreaves et al. (2014) modeled and computed the autorotation of a square flat plate by CFD (Computational Fluid Dynamics) - RBD (Rigid Body Dynamics) coupling method with RANS (Reynolds-Average Naiver-Stokes) model for turbulence simulation. Domenge et al. (2016) adopted the DDES (delayed-detached-eddy simulation) methodology and obtained more accurate predictions than the RANS method.

This work is motivated by the fact that only several selected rotating speeds have been considered in both experimental and computational studies for a foil rotating in a uniform cross flow as stated above. In other words, a complete picture for

the effect of rotating speed on vortex shedding characteristics, far-field wake pattern and aerodynamic performance still lacks, which is the main objective of this study. Therefore, we perform numerical simulations of a uniform cross flow past an elliptic foil rotating at $0 < \omega^* \leq 1$ and $Re = 100$, 200 and 300, as well as the thickness ratio of the foil $\beta = b/c = 0.125$, where b and c are the minor and major axial length of the elliptic foil respectively. Although the Reynolds number may not be very high, e.g. compared with vertical-axis wind turbine, it is a well-studied flow condition which is well within the regime of periodic vortex shedding of a uniform flow past a fixed circular cylinder. Thus, we hope the results from the present study could be indicative for applications in the Reynolds number range of $O(10^2 \sim 10^3)$, like insect-scale rotary wing or possible micro-wind energy harvester. The paper is arranged as follows. The numerical method and the validation study are introduced in section 2. The main results are given and discussed in section 3. The section 4 summarizes the main conclusions of the paper.

2. Numerical methods

2.1. Brief description

The two-dimensional incompressible Navier-Stokes equations

$$\frac{\partial u_i}{\partial t} + \frac{\partial \left(u_i u_j\right)}{\partial x_j} = -\frac{\partial p}{\partial x_i} + \frac{1}{Re}\frac{\partial^2 u_i}{\partial x_j^2} + f_i, \quad (i = 1, 2) \tag{1}$$

and the continuity equation

$$\frac{\partial u_i}{\partial x_i} = 0, \tag{2}$$

are solved numerically by a high-order numerical solver as well as a direct-forcing immersed boundary (IB) method for moving solid, where x_i is the ith Cartesian coordinate, u_i is the fluid velocity component in the ith direction, p is the pressure divided by fluid density, and f_i is the forcing term by solid to fluid (Uhlmann, 2005; Kempe and Fröhlich, 2012; Breugem, 2012). All the flow variables are normalized by reference length L_{ref} and velocity U_{ref}. Here we use the chord length c of the foil as L_{ref}, and the uniform inflow velocity U_∞ as U_{ref}. The Reynolds number is defined as $Re = U_{ref}L_{ref}/\nu$, in which ν is the fluid kinematic viscosity. A fourth-order accurate compact difference scheme is adopted for discretization of derivatives and interpolations on a staggered grid. Exact projection method is used for velocity-pressure decoupling. For temporal advancement, we implement the Adams-Bashforth scheme for the convection terms, and Crank-Nicolson scheme for the viscous terms to permit large time steps. The pressure Poisson equation is solved efficiently by the fast Fourier transform (FFT). The details of the current flow solver can be found in Hu et al. (2018).

The computational setup is shown in figure 2. The x and y denotes streamwise and transverse directions respectively. At the top and bottom boundaries, the free-slip and non-penetration velocity conditions are enforced. The uniform freestream condition is

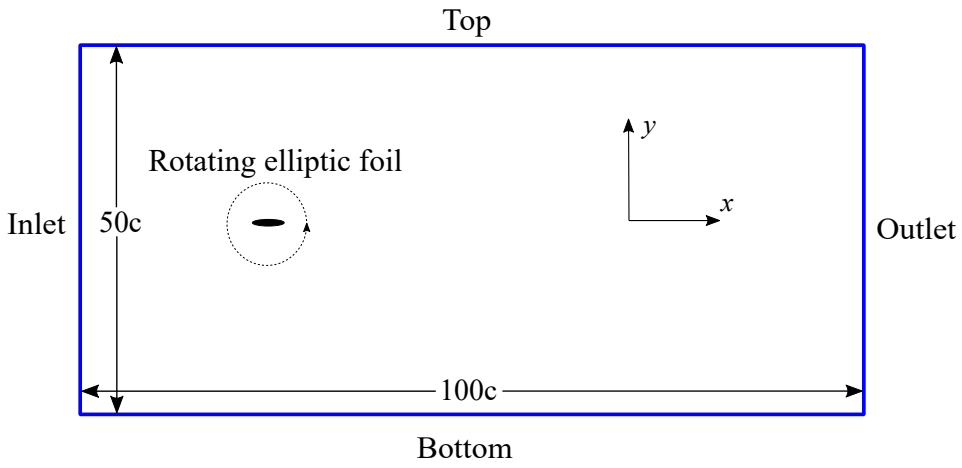

Figure 2. Computational domain and boundaries.

applied at the inlet boundary, and an outflow condition of $\partial_t u_i + U_\infty \partial_x u_i = 0$ at the outlet boundary. The domain is long and wide enough to eliminate the effect of outer boundaries on the interior of the flow.

2.2. Validation

The immersed boundary method is validated by two tests, i.e. a uniform flow past a fixed circular cylinder and an inline oscillating cylinder in a quiescent fluid, given in the Appendix in detail.

We further conduct a computational case of two-dimensional flow past a stationary elliptic foil with its major axis perpendicular to the freestream direction. The thickness ratio of the elliptic foil is $\beta = b/c = 0.25$. In contrast to a cylinder or sphere, the geometry of an ellipse is anisotropic and an approximate method is proposed to distribute the Lagrangian points uniformly on its surface, as required by the direct-forcing IB method (Uhlmann, 2005). Generally speaking, the arc length of an ellipse is calculated by the incomplete elliptic integral of the second kind via the built-in functionality *ellipticE* in Matlab. We subdivide the eccentric angle with an interval of 0.5° and determine the Lagrangian points for minimizing the errors to the targeting arc length. A maximum relative error of around 5% is obtained for distributing 64 points on an ellipse with thickness ratio of $\beta = 0.25$. In the present case, the Reynolds number is $Re = 200$, where $Re = U_\infty c/\nu$. The computational domain extends between $-25 \leq x/c \leq 75$ and $-25 \leq y/c \leq 25$, already shown in figure 2, of which the blockage is 2% to be small enough, the same as Thompson et al. (2014). The centroid of the foil is located at the origin of the coordinate system. The grid distribution is similar to the previous cylinder cases, namely $c/h = 25$ and 64 Lagrangian points on the foil surface. Table 1 shows the computed mean and root-mean-squared values of aerodynamic coefficients and the Strouhal number, as well as the computational result of Thompson et al. (2014), in which the authors adopted a high-order spectral-element method. The differences between present computation and Thompson et al.

Table 1. Mean and root-mean-squared (rms) values of aerodynamic coefficients and the Strouhal number of a uniform flow past a normal elliptic foil.

	$\bar{C}_L$	$\bar{C}_D$	$C_{L,\mathrm{rms}}$	$C_{D,\mathrm{rms}}$	St
Thompson et al. (2014)	-	2.1615	-	-	0.1611
Present	-0.0144	2.1911	0.4726	0.1640	0.1623

(2014) for the mean drag coefficient and the Strouhal number are less than 2% and 1%, respectively. Therefore, we adopt this computation setup in the present study, which should be sufficient to yield accurate results.

Secondly, we compute a two-dimensional uniform flow past a rotating elliptic foil with $\beta = 0.125$ at $\omega^* = 0.417$ and $\omega^* = 1.667$, comparing with the experimental measurement by Lua et al. (2010), in which flow field data is available. The Reynolds number is $Re = 200$. We use the same computational setup as the fixed case, i.e. domain size and grid distribution. The non-dimensional time is defined as $t^* = t/T_r$, in which the physical time t is normalized by the rotation period $T_r = 2\pi/\omega$. Reasonable agreements between the current computation and PIV measurement of Lua et al. (2010) (not shown here for saving space) can be found. Various shed vortices observed in the experiment have been successfully reproduced in the present simulation. Thus, the numerical methods and formulations adopted in the present study has been well validated through numerous tests.

3. Vortex detection method

The detection of vortex is crucial in understanding the flow physics and flow control, which is always one long-standing topic in fluid dynamics research. There are numerous methodologies that could be utilized for vortex detection in two-dimensional flow ~~data~~, e.g., the classical ones as introduced by Vollmers (2001), i.e. the streamlines method, the cross-section lines method, the vorticity moments method, the vorticity contour lines method and so on, as well as some modern developments like the wavelet-based method (Schram et al., 2004; Varun et al., 2008; Wang et al., 2015), the Γ_2 method (Graftieaux et al., 2001; Simpson et al., 2018), among many others. ~~In~~ three-dimensional flows, people have realized the drawbacks of the vorticity-based method, that a shear layer can not be distinguished from a vortex since both of which could have high vorticity, thereafter a number of vortex identification criteria have been proposed, see Chakraborty et al. (2005) and references therein. In this work, we adopt the Q criterion (Hunt et al., 1988), i.e., the second invariant of the velocity gradient tensor, to detect vortex which are located at $Q > 0$. In a two-dimensional Cartesian coordinate, $Q = (\partial_x u)(\partial_y v) - (\partial_x v)(\partial_y u)$, where u and v are the flow velocity components in x and y directions, respectively. In fact, it can be easily proved that the Q criterion is identical to other similar schemes (e.g., λ_2, Δ) in two dimension.

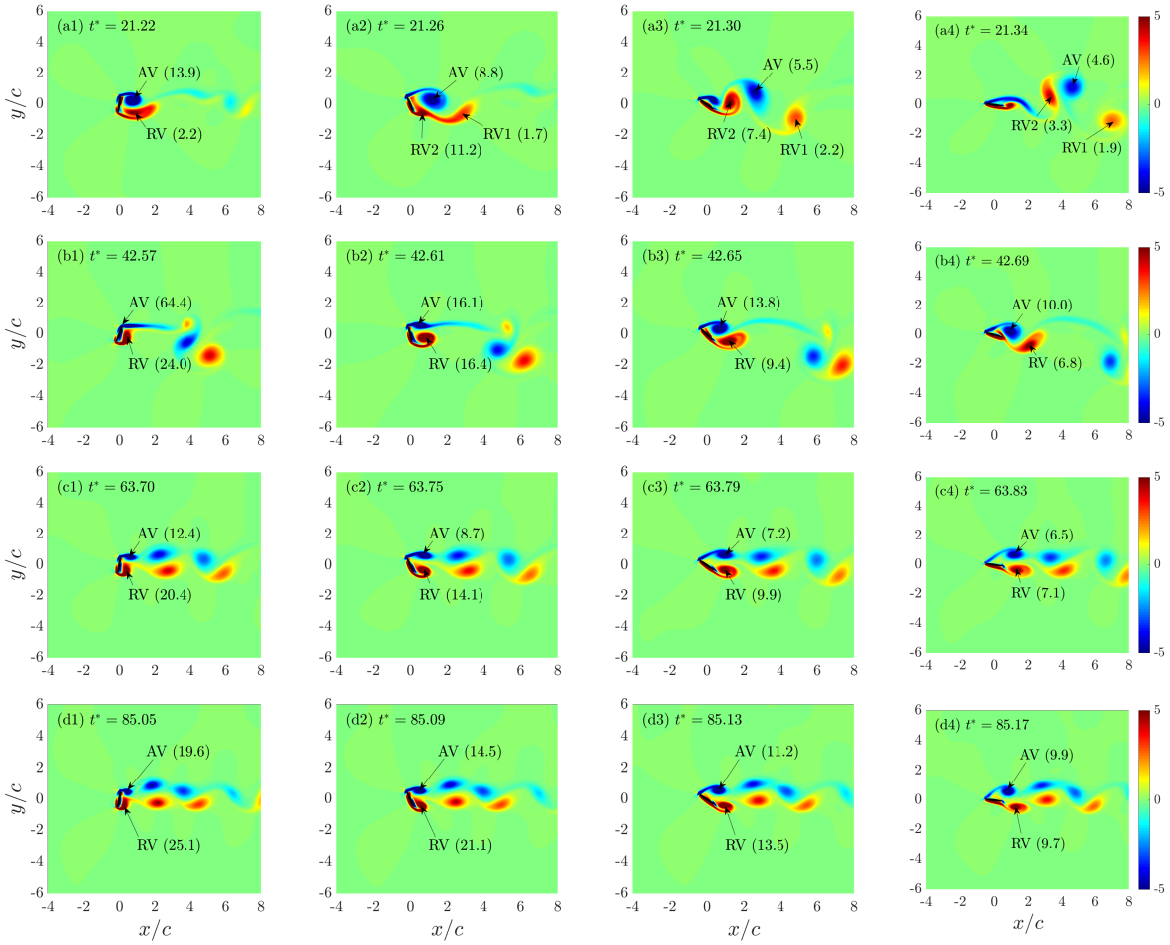

Figure 3. Vortex shedding process during foil rotation (Re = 200): (a) ω^* = 0.10; (b) ω^* = 0.20; (c) ω^* = 0.30; (d) ω^* = 0.40. The local maximum normalized Q value of a vortex is supplemented in the bracket behind it.

4. Results and analysis

4.1. Vortex shedding characteristics

In this section, we analyze the near-body vortex shedding characteristics over a rotating elliptic foil at different rotating speeds at Re = 200. There are already several studies dedicated on this problem (Lugt and Ohring, 1977; Lua et al., 2010; Hu, 2015; Naik et al., 2017; Lua et al., 2018; Lu et al., 2018) but only limited to several typical rotating speeds. The simulations were carried out for long enough time to reach a stably periodic status (by monitoring drag, lift and torque coefficients). The vorticity fields shown afterwards are all normalized by the reference velocity $U_{ref} = U_\infty$ and reference length $L_{ref} = c$.

Figure 3 displays typical instantaneous vorticity fields at four low rotating speeds, i.e. ω^* = 0.10, 0.20, 0.30 and 0.40. There are some common features among them. When the foil is almost normal to the incoming flow, see figure 3 (a1), (b1), (c1) and (d1), an advancing vortex (AV) and a retreating vortex (RV) shed from the advancing and retreating edges of the foil, respectively. This is simply because a flow separates from

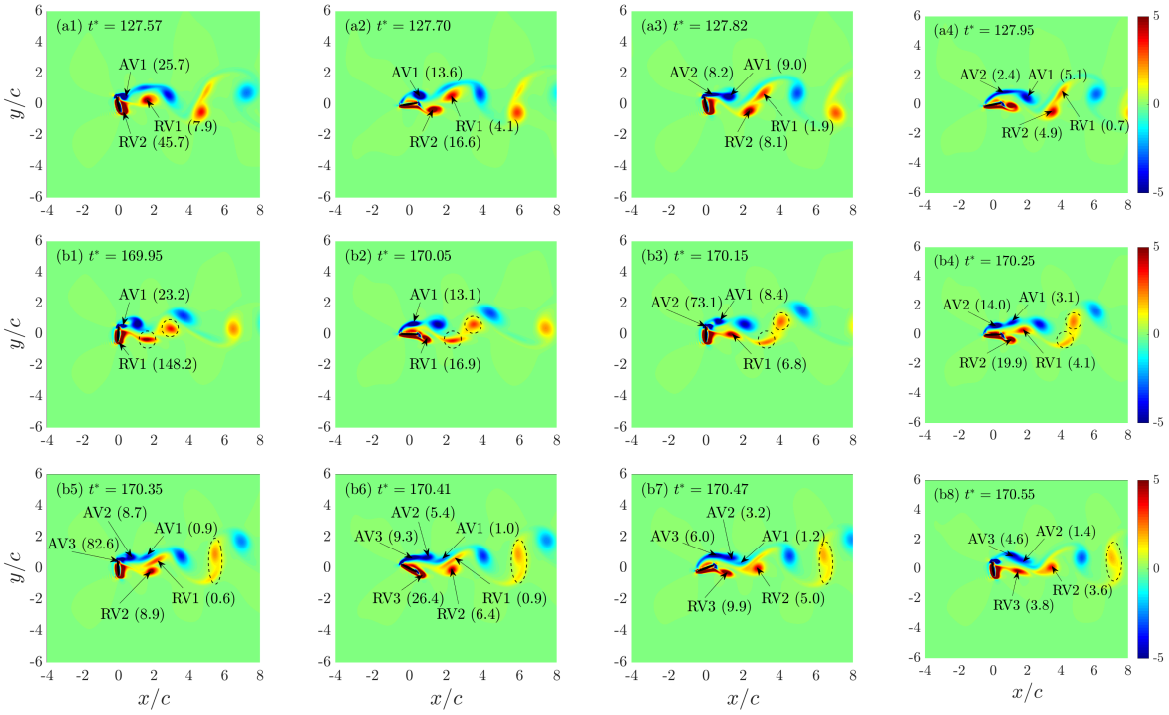

Figure 4. Vortex shedding process during foil rotation (Re = 200): (a) ω^* = 0.60; (b) ω^* = 0.80. The local maximum normalized Q value of a vortex is supplemented in the bracket behind it.

two sharp edges at a large angle of attack. At $\omega^* = 0.10$, the foil rotates quite slowly so that the AV and RV have enough time to convect downstream, as in figure 3 (a2). At this instant, a second retreating vortex is generated at the retreating edge of the foil which is termed by RV2, and the previous RV is termed by RV1 instead. Afterwards, RV2 and AV form a compact counter-rotating vortex pair, which is convected downstream and slightly upwards above the centerline, while the RV1 moves a little downwards below the centerline, as shown in figure 3 (a3) and (a4). This vortex shedding process repeats every half rotation. It is seen that the intensities of the vortex decrease with time that indicates the vortices diffuse during their movements, and the maximum Q values of AV and RV2 are obviously stronger than that of RV1. At $\omega^* = 0.20$, the foil rotates two times faster, and we could not identify any RV2 at this condition. While AV and RV form a pair of counter-rotating vortex and move downstream, slightly downwards below the centerline, which is depicted in figure 3 (b2), (b3) and (b4). At higher rotating speeds, as those in figure 3 (c) and (d) with $\omega^* = 0.30$ and 0.40, there is also no obvious second vortex (RV2) that can be observed anymore, and only a pair of AV and RV sheds in each half rotation. The vortical flows are generally periodic with the period being a half rotation. One interesting finding is that the intensities of the vortices at higher foil rotating speed are stronger, which could be probably attributed to larger relative tip-to-flow speed difference. This was also observed by Lua et al. (2010).

Figure 4 shows the vorticity fields at two typically higher rotating speeds, i.e. $\omega^* = 0.60$ and 0.80. From figure 4 (a), it is seen that AVs/RVs shed during adjacent two

half rotations at $\omega^* = 0.60$ may evolve into a dominant pair of AV/RV, which is actually the stronger AV1/RV2 other than the weaker AV2/RV1, the latter will be stretched and diffused much more quickly. Thus, the vortex shedding period at $\omega^* = 0.60$ is one complete rotation actually. At $\omega^* = 0.80$, we display typical vorticity distributions during one and a half rotation. It is observed that three AVs (AV1, AV2 and AV3) are shed and evolve into a single AV at the end of the process, which is possibly stronger AV3/AV2 while AV1 can not be identified, see figure 4 (b6) to (b8). At the same time, stronger RV2/RV3 will also evolve into a single RV finally, and RV1 is very weak and can not be detected anymore at the end. The evolving process of RV2/RV3 into a single RV in the previous period is illustrated by the dashed circles in figure 4 (b1) to (b8).

Lua et al. (2010) firstly reported the phenomenon that AV could stay above the foil for a period of time if the rotation speed is large enough, and they named it as "hovering vortex". This phenomenon has also been confirmed by later studies (Hu, 2015; Naik et al., 2017; Lua et al., 2018). Here we attribute this phenomenon to the variation of $\eta = T_s/T_c$, i.e. the ratio of vortex shedding time scale (T_s) to vortex convection time scale (T_c). The vortex convection time scale T_c could be approximated by the ratio of a reference distance $L_c = c$ to vortex convection velocity U_c, the latter could be approximated by the freestream velocity U_∞, so $T_c \approx L_c/U_\infty$. We can reasonably assume that T_c is a constant, since L_c and U_∞ are both constants. Therefore, the variation of η is purely determined by the vortex shedding time scale T_s. As ω^* increases, the vortex shedding period is reduced so that η decreases. Therefore, at a low rotating speed, the time scale ratio η is high since the vortex shedding frequency is low, and the vortices shed among adjacent rotations are not directly interacting with each other, therefore there is no hovering vortex. If η is very small, which indicates that the foil rotates very fast, an AV may not have enough time to move downstream, then a new AV is shed and thus likely interacts with the previous one to form a single AV. From this observation, we could speculate that the hovering vortex phenomenon is simply because a foil is rotating too fast, that AVs do not have enough time to move downstream.

4.2. Far-field vortical wakes

In this section, the far-field wakes behind the rotating foil will be discussed, which have not been reported before. Here the "far-field" is against "near-body", and could be roughly defined as the region of $x/c > 5$ in this work, since the near-body vortex shedding process in 4.1 demonstrates that the most intense vortex-vortex interactions occur at $x/c < 5$.

Figure 5 shows the far-field wakes at all rotating speeds up to a downstream location of about $x/c = 70$ at $Re = 200$. At $\omega^* = 0.10$, we already know that a pair of counter-rotating vortex and a relatively strong individual RV are shed in the near-body region of the flow, as displayed in figure 3 (a). From figure 5 (a), we can see that the vortex pair rotates first and then appears to achieve a stable configuration (nearly horizontal) in the far field. On the other hand, the individual RV with a weak AV is a little behind the

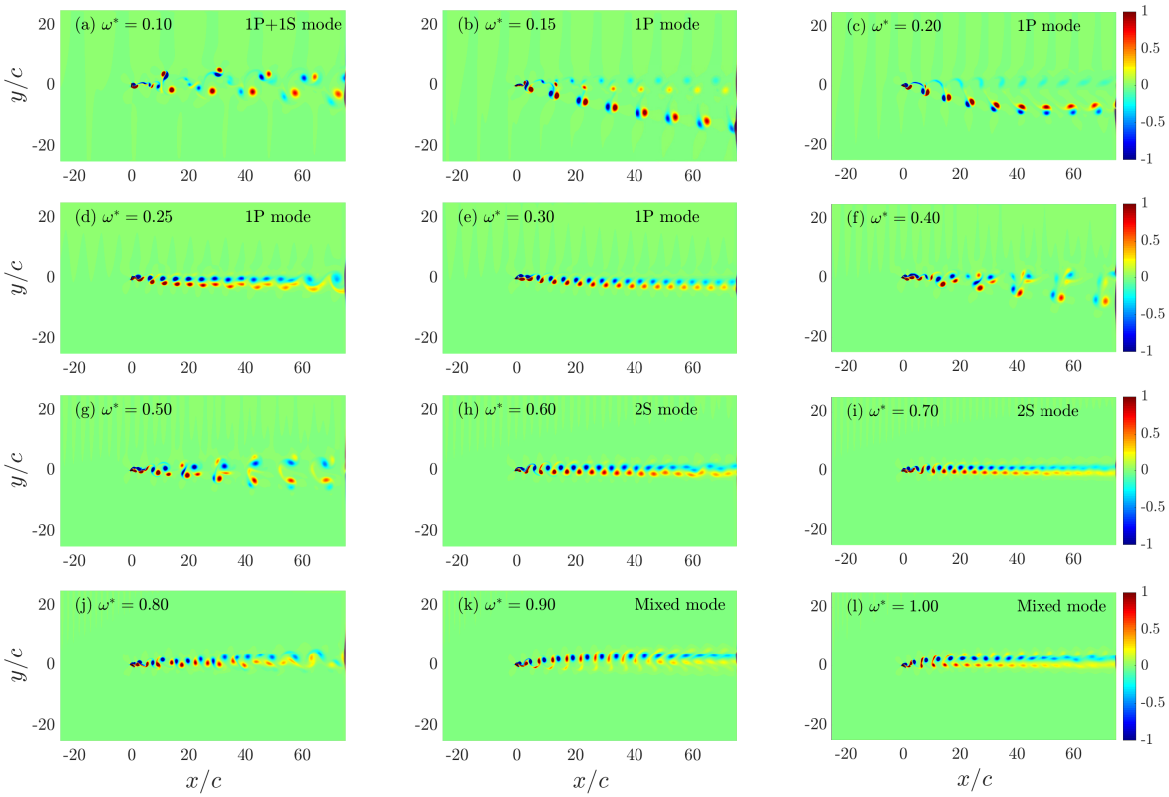

Figure 5. Far-field vortical wake behind the rotating foil at $Re = 200$.

corresponding vortex pair in streamwise. This far-field wake pattern could be categorized into the 1P+1S mode (hereafter "P" and "S" are short for pair and single respectively), following the wake mode nomenclature of circular cylinder in vortex-induced vibration (Williamson and Roshko, 1988; Govardhan and Williamson, 2000). The wake patterns are quite similar at $\omega^* = 0.15$ and 0.20, see figure 5 (b) and (c). The strong vortex pair of AV and RV moves downstream and deflects downwards, in other words visible wake deflections are observed. We could ascribe this wake pattern to the 1P mode since the other vortex pair are much more weaker. In figure 5 (d) and (e), i.e. $\omega^* = 0.25$ and 0.30, the downward wake deflection reduces, and a distinct vortex pair row is formed in the wake, which could also be classified into the 1P mode. At $\omega^* = 0.40$ and 0.50, since the adjacent vortex pairs are getting closer, the mutual interactions among them make the wake much more complex in the middle region, therefore the far-field wake is also somewhat irregular. At $\omega^* = 0.60$ and 0.70, the wake becomes more symmetric in a form of staggered vortex street, like that behind a circular cylinder, and the far-field wake could be regarded as the 2S mode. It may be questioned that the wake patterns at $\omega^* = 0.60$ and 0.70 look quite similar to that of $\omega^* = 0.30$. However, they are actually different. From the near-body vortex shedding process, we know that a pair of AV and RV is generated during a half rotation at $\omega^* = 0.30$, and distinct vortex pairs can be visibly seen in figure 5 (e), i.e., one AV (RV) is closer to one of the adjacent RV (AV) than the other one. However, it is not the case at $\omega^* = 0.60$ and 0.70, since single AV

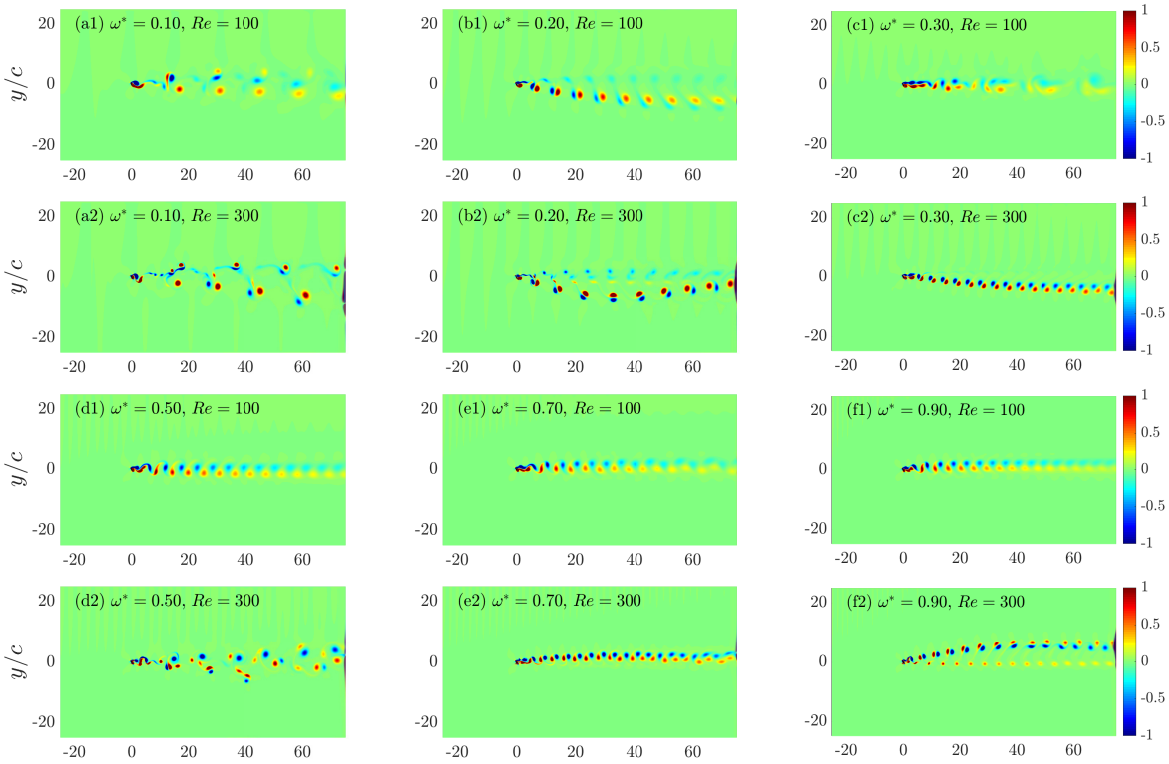

Figure 6. Far-field vortical wake behind the rotating foil at $Re = 100$ (a1-f1) and $Re = 300$ (a2-f2).

and RV are shed during one rotation, in which no vortex pair is formed. From figure 5 (h) and (i), it is seen that AVs and RVs are almost uniformly organized in space. The symmetry of the wake seems to be broken again at $\omega^* = 0.80$ in figure 5 (j) and the wake pattern is irregular especially in far field. The deflection of the wake is obviously inverse at high rotating speeds, i.e. $\omega^* = 0.90$ and 1.00, in which the wake is deflected upwards. The far-field wake pattern is recognized as a mixed mode, because the wake transits from 1P+1S mode to 2S mode at $\omega^* = 0.90$ after $x/c \sim 30$ and $\omega^* = 1.00$ after $x/c \sim 15$.

Figure 6 shows the far-field vortical wakes at $Re = 100$ and 300, demonstrating the Reynolds number effect. In general, the intensity of the vortices in the wake increases with Reynolds number, which is evident by comparing figure 5 and figure 6 at the same rotating speed. The wake patterns at $Re = 300$ are in good coincidence with $Re = 200$, while those at $Re = 100$ are somewhat different. For instance, at $\omega^* = 0.10$, the 1P+1S mode can still be observed at $Re = 300$, but it can hardly be identified at $Re = 100$ where the vortices diffuse quite quickly in the far field. The vortical wake at $\omega^* = 0.30$ is 1P mode with obvious deflection when $Re = 200$ and 300, while which is not very regular at $Re = 100$. Furthermore, at $Re = 100$ with $\omega^* \geq 0.50$, the vortical wakes are 2S mode with limited deflection. And the wake deflection is more elevated at higher Reynolds numbers.

4.3. Wake deflection

As we have shown previously, the far-field wake of a foil rotating in a uniform flow may be deflected at particular rotating speed, which could be crucial to the aerodynamic performance of the foil. For example, the asymmetric wake can significantly alter the thrust and propulsive efficiency of a flapping foil (Jones et al., 1998; Heathcote and Gursul, 2007; Godoy-Diana et al., 2008, 2009; Zheng and Wei, 2012; Zhu et al., 2014). In this subsection, we will inspect the wake deflection through mean streamwise flow velocity deficit.

Figure 7 shows the time-averaged streamwise flow velocity fields with different rotating speeds at $Re = 200$, from which one can simply characterize the wake deficit and deflection. At $\omega^* = 0.10$ in figure 7 (a), the wake is likely symmetric at $x/c < 10$, but expands more upwards in far field. The wake is more obviously deflected downwards at $\omega^* = 0.15$, and bifurcated into two branches due to two vortex pair rows, as displayed in figure 7 (b). The wake deficit pattern of $\omega^* = 0.20$ is similar to that of $\omega^* = 0.15$, except that the bifurcation is not evident anymore. At $\omega^* = 0.25$ in figure 7 (d), the velocity deficit is stronger, the wake is more compact and the deflection is reduced, as a result of the compact vortex pattern in the wake. The scenario is similar at $\omega^* = 0.30$. A bifurcated wake arises again at $\omega^* = 0.40$, which is due to the vortex interaction and intermittent merging. In the range of $\omega^* = 0.50 \sim 1.00$, it is seen that a transition of wake deflection from downwards to upwards happens, and the wake is almost not deflected at $\omega_c^* \approx 0.60$, as shown in figure 7 (h).

Figure 8 (a) displays the streamwise variation of the deflected wake center, which is defined as the y location of the maximum velocity deficit at each x position, at different rotating speeds corresponding to figure 7. It is shown that the wake is downwards deflected at $\omega^* < 0.6$, and upwards deflected at $\omega^* \geq 0.6$. The wake deflection behavior can be interpreted by the orientation of the vortex pair, as sketched in figure 8 (b) and (c). If the anticlockwise vortex is on the left side of the clockwise vortex, the vortex pair (or vortex dipole) will induce an upward flow to make the wake deflected upwards, as shown in figure 8 (b). On the other hand, the wake will be downwards deflected if the vortex pair induce a downward flow, as in figure 8 (c). This interpretation has widely been used in the analysis of wake deflection in flow over a flapping foil (Godoy-Diana et al., 2009; Zheng and Wei, 2012; Zhu et al., 2014). However, we note that if the vortex strength is not equal, it may induce the rotation of the vortex pair, e.g. figure 5 (a), which results in the strong variations of the wake center curve at $\omega^* = 0.10$, as shown in figure 8 (a).

4.4. Aerodynamic performance

In this subsection, we focus on the aerodynamic force and torque acting on the rotating foil. The definitions of the aerodynamic coefficients are

$$C_L = \frac{L}{(1/2)\rho U_\infty^2 c}, \tag{3}$$

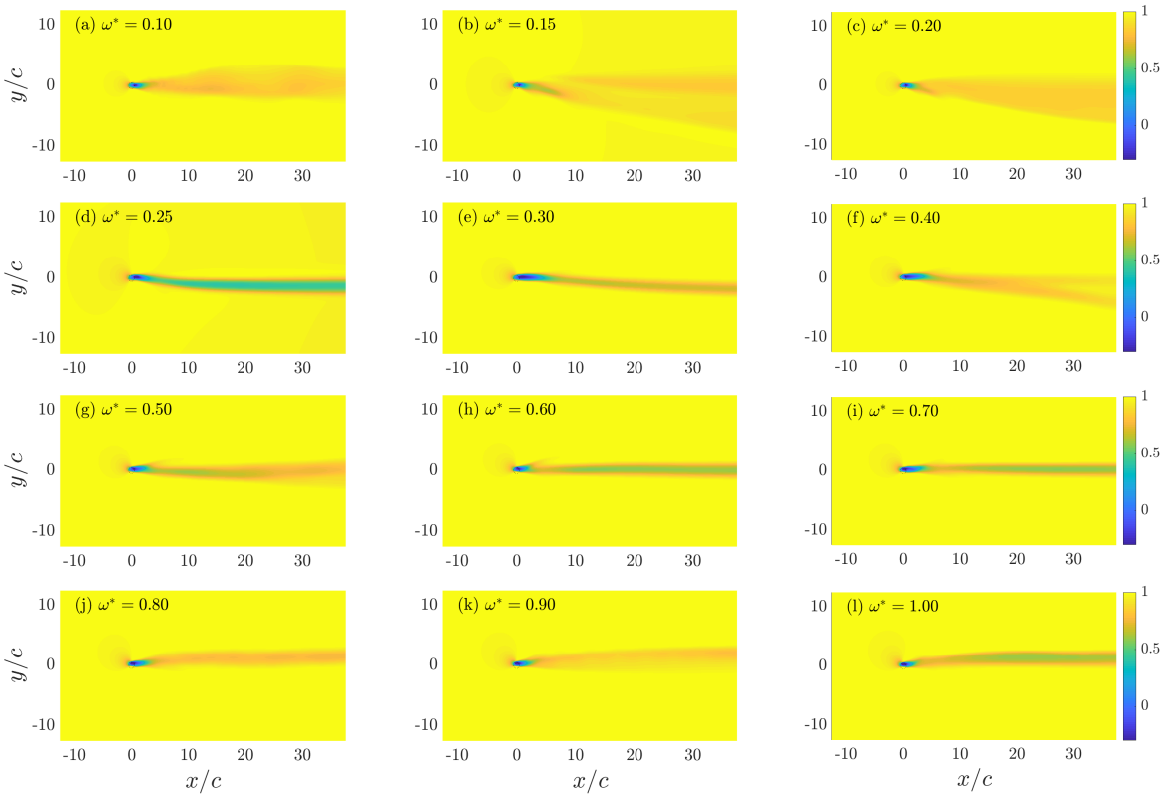

Figure 7. Time-averaged streamwise velocity fields at $Re = 200$.

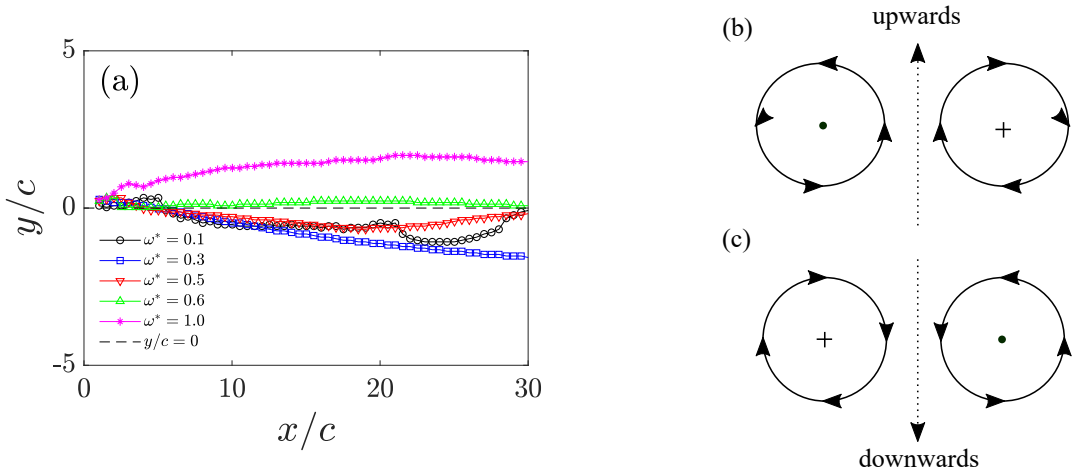

Figure 8. (a) Streamwise variation of the deflected wake center at $Re = 200$. (b) The vortex pair induced upward or downward flow.

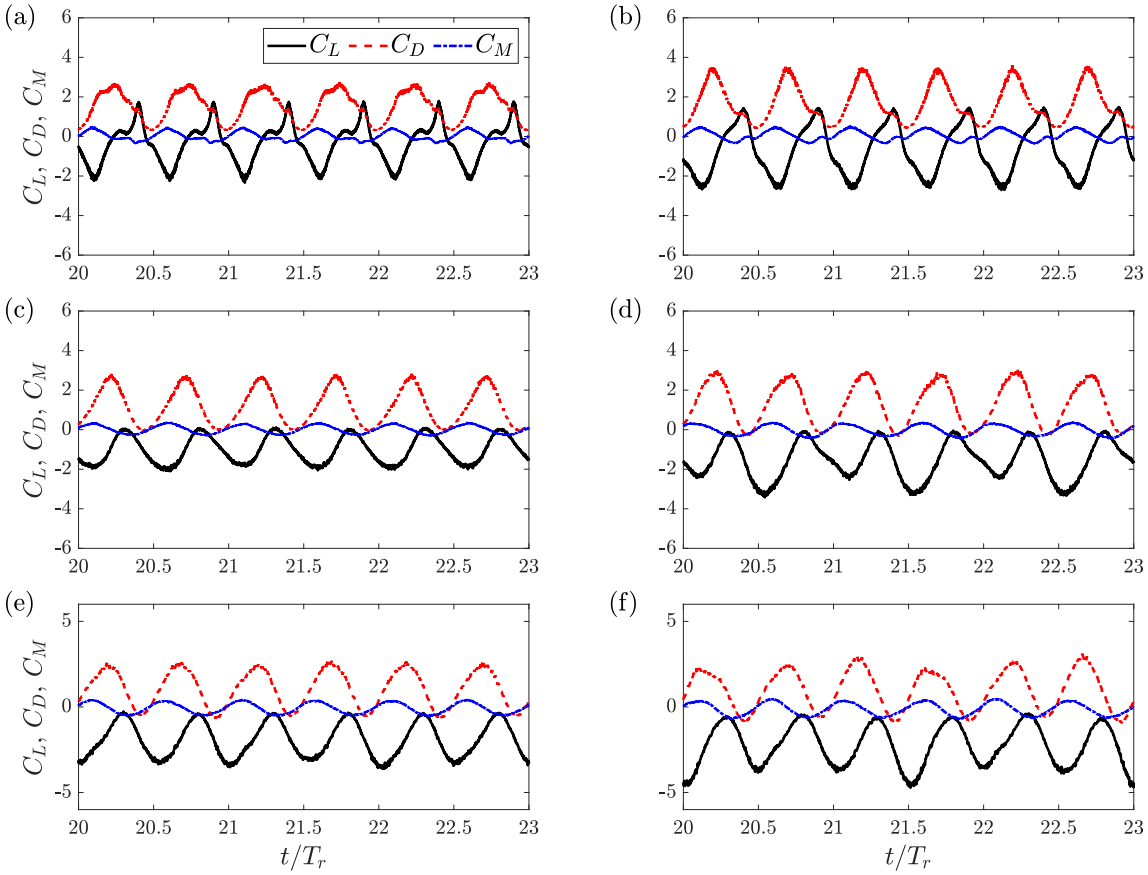

Figure 9. Time histories of lift, drag and torque coefficients (Re=200): (a) $\omega^* = 0.10$; (b) $\omega^* = 0.20$; (c) $\omega^* = 0.30$; (d) $\omega^* = 0.50$; (e) $\omega^* = 0.70$; (f) $\omega^* = 0.90$.

$$C_D = \frac{D}{(1/2)\rho U_\infty^2 c}, \tag{4}$$

$$C_M = \frac{M}{(1/2)\rho U_\infty^2 c^2}, \tag{5}$$

where L, D and M are the lift, drag and torque exerted on the foil by fluid flow, respectively. The torque M is calculated with respect to the geometric center of the foil.

Figure 9 shows the instantaneous lift, drag and torque coefficients at several typical rotating speeds. It is seen that the period of all the aerodynamic coefficients is approximately a half rotation ($T = T_r/2$) at $\omega^* \leq 0.30$, which is the same as that of the vortex shedding. At $\omega^* = 0.50$, it seems that the half rotation period increases to one rotation period for aerodynamic coefficients especially the lift coefficient, namely $T = T_r$. It is simply because of the occurrence of the intermittent vortex merging or diffusing. At higher rotating speed, e.g. $\omega^* = 0.90$, due to the vortex merging among one and a half rotation, the periods of the aerodynamic coefficients also increase to one and a half rotations ($T = 1.5T_r$). In general, the period of aerodynamic coefficient is in accordance of the vortex shedding. In order to accurately quantify the period of

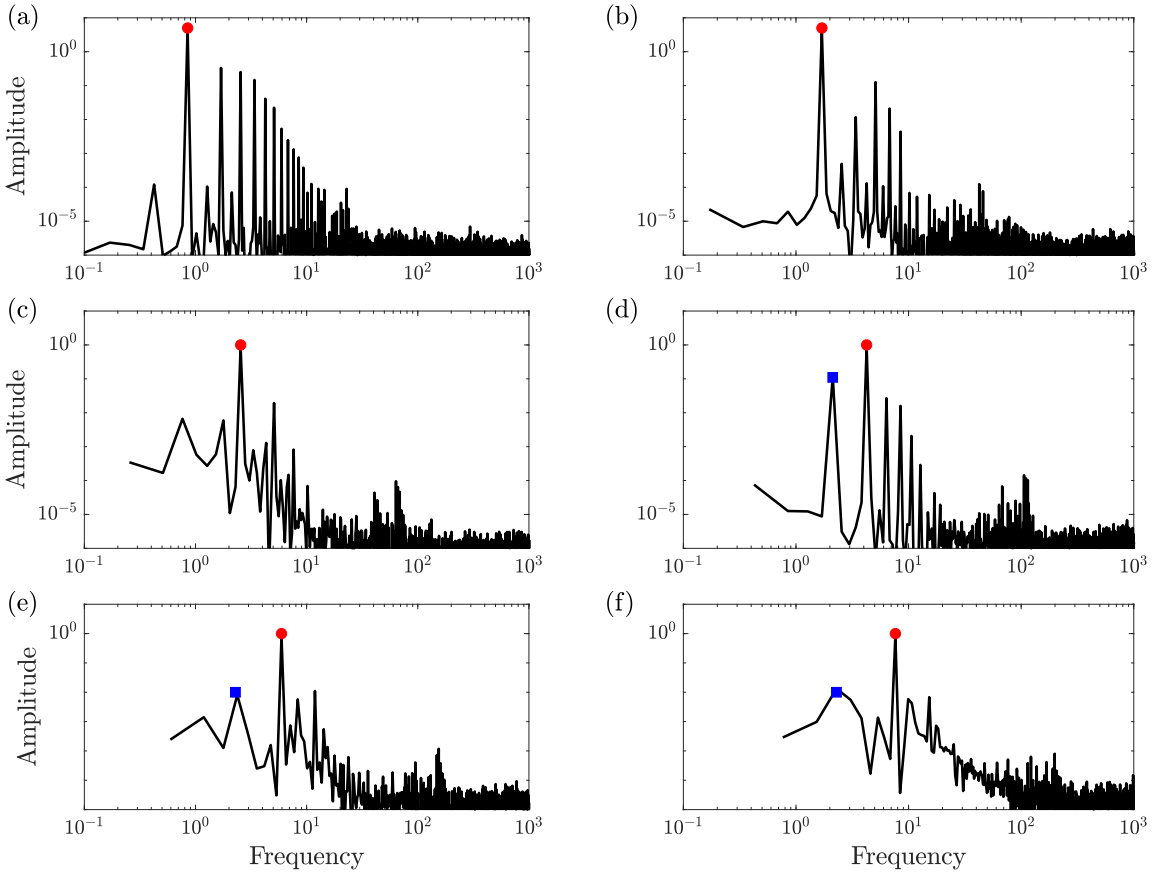

Figure 10. Frequency spectrum of lift ($Re = 200$): (a) $\omega^* = 0.10$; (b) $\omega^* = 0.20$; (c) $\omega^* = 0.30$; (d) $\omega^* = 0.50$; (e) $\omega^* = 0.70$; (f) $\omega^* = 0.90$.

aerodynamic force, we calculate the frequency spectrum of lift using FFT at different rotating speeds, shown in figure 10. The most dominant spectral peak is denoted by the red circle, which corresponds to the half rotation period in all cases. This result is not surprising because of good periodicity of the lift. On the other hand, we also highlight the second spectral peak by the blue square. At $\omega^* = 0.50$ and 0.70, the period of the second peak corresponds to T_r, consistent with the rough observation of instantaneous aerodynamic coefficients. Furthermore, at $\omega^* = 0.90$, the second peak shifts to a period of $1.5T_r$, also in agreement with above observation. As the rotating speed increases to $\omega^* > 1.0$, we could imagine that the second frequency (period) of the lift will decrease (increase) successively.

Figure 11 displays the time-averaged lift, drag and torque coefficients with respect to the rotating speed at all three Reynolds numbers. The magnitude of the mean lift coefficient increases monotonically with the rotating speed. The lift coefficient is almost the same at $Re = 200$ and 300 when $\omega^* \geq 0.20$ and larger than that at $Re = 100$. The variation of the mean drag coefficient is not monotonic. The mean torque coefficient increases first, and then decreases with rotating speed, the maximum of which is at $\omega^* \approx 0.20$. We note that there is a significant drag reduction between $\omega^* = 0.20$ and

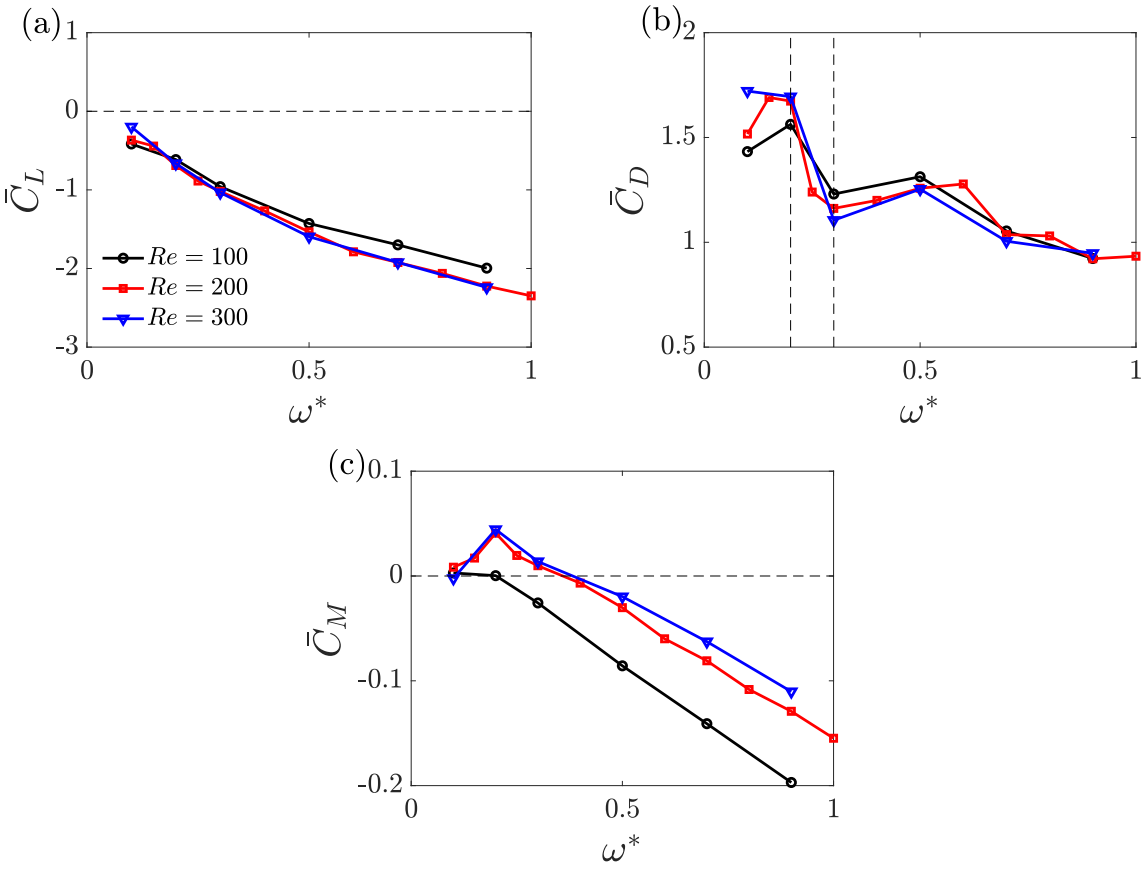

Figure 11. Variations of the mean lift (a), drag (b) and torque (c) coefficients with rotating speed.

$\omega^* = 0.30$, as indicated by two dashed lines in figure 11 (b). This drag reduction is closely related to the wake deflection, or more specific, the orientation of the dominant vortex pair in the wake. It is clearly seen that the wake pattern at $\omega^* = 0.25$ resembles a "reversed Bénard-von Kármán vortex street" very much, see figure 5 (d), thus a forward flow induced by the wake could reduce the drag effectively (Godoy-Diana et al., 2009). In figure 11 (c), it is interestingly found that the torque coefficient is positive in a low rotating speed regime $\omega^* < \omega_t^*$, meaning that the flow can promote the rotation of the foil and the fluid energy could be harvested in this regime. And the width of this regime increases with Reynolds number, at least in the range of Reynolds number considered here. On the other hand, the aerodynamic torque is negative and energy input is needed to sustain the rotation of the foil at $\omega^* > \omega_t^*$. The curve in figure 11 (c) could be regarded as an inverse "Riabouchinsky curve", where the driving torque is balanced by the aerodynamic torque for a foil rotating at a constant speed. It is further noted that $\omega^* = \omega_t^*$ could be regarded as the "stable autorotation rate" in the "Riabouchinsky curve", as in figure 1. However, we did not find the "minimum autorotation rate" from the present numerical simulation, which may be even smaller than $\omega^* = 0.10$, or does not exist in this low Reynolds number range.

5. Conclusions

The flow over an elliptic foil rotating at low Reynolds numbers of $Re = 100 \sim 300$ has been investigated through numerical simulations. The non-dimensional rotating speed is in the range of $0 < \omega^* \leq 1.0$, and its effects on the vortex shedding characteristics, far-field wake patterns and aerodynamic performances are studied.

The main conclusions are summarized here. At low rotating speeds, e.g. $\omega^* \leq 0.20$, besides the main AV (advancing vortex) and RV (retreating vortex), there are second weak vortices shed in a half rotation. The far-field wake is deflected downwards and comprised of two rows of strong and weak counter-rotating vortex pairs. At $\omega^* \approx 0.20 \sim 0.30$, only a pair of AV and RV is shed during a half rotation, and the wake exhibits a slightly downwards deflected row of vortex pairs. At $\omega^* \approx 0.30 \sim 0.60$, the wake tends to be symmetric in the crossing direction. At $\omega^* \geq 0.60$, the adjacent AVs (RVs) could evolve into a single AV (RV). With increasing the rotating speed, more vortices will participate in this process due to the relative small time scale ratio η between vortex shedding and vortex convection. The far-field wake is deflected upwards instead. The mean lift coefficient increases monotonically with the rotating speed. The mean drag force is significantly reduced at $\omega^* = 0.25$ where the wake pattern resembles a "reversed Bénard-von Kármán vortex street", i.e. a forward flow is induced by vortex street and the drag exerted on the object is reduced (Godoy-Diana et al., 2009). At small rotating speed, the fluid flow could promote the rotation of the foil since the torque coefficient is positive. As Reynolds number increases, both the intensities of wake vortices and the degree of wake deflection increase, as well as the magnitude of lift coefficient and the width of the positive-torque regime.

~~Furthermore, we would like to address the two-dimensional nature of the flow.~~ As discussed by Lua et al. (2018), in the parameter space investigated here, the flow could be largely two-dimensional since the separation point is fixed at a rotating thin elliptic foil. In our previous three-dimensional simulation (Hu, 2015), it could also be observed that the flow is largely two-dimensional with a moderate wing aspect ratio of 6, i.e. spanwise vortices dominate in the wake. However, it should be interesting and useful to inspect the three-dimensional features of the flow in future.

~~At last,~~ although many investigations have been conducted on flow over a rotating bluff body, like rotating circular cylinder (Kang et al., 1999; Stojković et al., 2002; Mittal et al., 2004; Rao et al., 2015) or rotating sphere (Best, 1998; Giacobello et al., 2009; Poon et al., 2014), it should be noted that there exist non-negligible difference between them and the flow around a rotating thin foil. To be more specific, the wake of the flow past a rotating bluff body could be classified into Bénard-von Kármán vortex street type, while that of flow past a rotating thin foil is prevailed by tip vortices shed from two sharp edges of the foil (Lua et al., 2018).

Acknowledgments

This work was financially supported by grants from the National Natural Science Foundation of China (Nos. 11502185 and 11972175) and Natural Science Basic Research Plan in Shaanxi Province of China (No. 2016JQ1004).

Appendix A. A circular cylinder in a uniform flow

A uniform flow past a fixed circular cylinder is simulated to validate the present implementation of the direct-forcing IB method. The Reynolds number $Re = U_\infty D/\nu = 100$, in which U_∞ is the freestream flow velocity, D is the diameter of the circular cylinder, and ν is the kinematic viscosity of the fluid. The size of computational domain is $50D \times 50D$, and the centroid of the cylinder is located at 12.5D in streamwise (x) from the inlet and symmetrically in transverse (y). The grid number is 1000×1000 in x and y directions respectively and distributed uniformly. Hence the ratio of the cylinder diameter to the grid size D/h is 25, in comparison, which is 38.4 in Uhlmann (2005). The number of Lagrangian points on the surface of the cylinder is set to be 64 according to Uhlmann (2005). A Dirichlet inflow boundary condition ($u/U_\infty = 1, v = 0$) is adopted at the inlet, free-slip and symmetric conditions at the top and bottom boundaries, and a convective boundary condition at the outlet. The computational time step is $\Delta t \approx 0.01D/U_\infty$ and the CFL number is about 0.5.

Table A1 displays the simulation results using the present direct-forcing IB method and some reference data from the literature. We also made comparison between the second-order accurate central difference scheme and the fourth-order accurate compact difference scheme. The definitions of the mean lift and drag coefficients and the Strouhal number are

$$\bar{C}_L = \frac{\bar{L}}{(1/2)\rho U_\infty^2 D}, \tag{A.1}$$

$$\bar{C}_D = \frac{\bar{D}}{(1/2)\rho U_\infty^2 D}, \tag{A.2}$$

$$St = \frac{fD}{U_\infty}, \tag{A.3}$$

where $\bar{L}$ and $\bar{D}$ are time-averaged lift and drag, and f is the natural vortex shedding frequency evaluated by the dominant frequency of the lift force. C'_L and C'_D are the maximum deviations of the lift and drag coefficients from the mean values.

In particular, the present numerical method is similar to Uhlmann (2005) with improvement of additional sub-iterations in the IB step (Kempe and Fröhlich, 2012; Breugem, 2012; Zhou and Fan, 2014). Kim et al. (2001) adopted a finite-volume direct-forcing IB method with a mass source/sink. And Li et al. (2016) developed an efficient IB projection method. It is seen from table A1 that the present simulation results using high-order difference scheme are in better agreements with the reference data, especially

Table A1. Simulation results for a uniform flow past a fixed circular cylinder at $Re = 100$.

	$\bar{C}_D$	C'_L	St
Present (2nd order)	1.45	0.39	0.165
Present (4th order)	1.41	0.35	0.165
Kim et al. (2001)	1.33	0.32	0.165
Uhlmann (2005)	1.45	0.34	0.169
Li et al. (2016)	1.36	0.33	0.165

for the mean drag coefficient and the lift coefficient fluctuation. Also, even with a coarser spatial resolution, the present results are better than that of Uhlmann (2005) due to more accurate numerical scheme and improvement of the IB method.

Appendix B. An inline oscillating cylinder

In order to verify the applicability of the present numerical method for the moving boundary problem, we perform a computational study on the unsteady flow around an inline oscillating cylinder in a quiescent fluid. The cylinder undergoes a sinusoidal oscillation as

$$x_c(t) = -A_m \sin(2\pi f t), \tag{B.1}$$

where x_c is the centroid of the cylinder, A_m is the oscillating amplitude, f is the oscillating frequency and t is the time. The two controlling dimensionless parameters are the Reynolds number ($Re = U_m D/\nu$) and the Keulegan-Carpenter number ($KC = 2\pi A_m/D$), in which $U_m = 2\pi A_m f$. The phase angle ϕ is defined by $\phi = 2\pi f t$. Here we compute the flow at $Re = 100$ and $KC = 5$, for which the benchmark data is available (Dütsch et al., 1998).

The computational domain size and grid distribution are the same as the stationary cylinder case, while the centroid of the cylinder is located in the center of the domain. The ratio of the cylinder diameter to the grid size ratio is still $D/h = 25$. The number of Lagrangian points on the cylinder surface is also 64. Dirichlet boundary conditions ($u = v = 0$) are applied at all four outer boundaries. The CFL number is kept to be 0.5.

Figure B1 displays the computed time history of drag coefficient of the inline oscillating cylinder. In comparison with the reference result (Dütsch et al., 1998), reasonable agreement can be observed. It is also noted that there exist high-frequency oscillations in the drag curve, which is a common problem in the direct-forcing IB method (Uhlmann, 2005; Yang et al., 2009). Here we do not eliminate it because the oscillation amplitude is very small compared to the absolute value of the drag. To further illustrate the present computation with experimental data, velocity profiles at four x cross-sections and three different phase angles are displayed in figure B2. Excellent

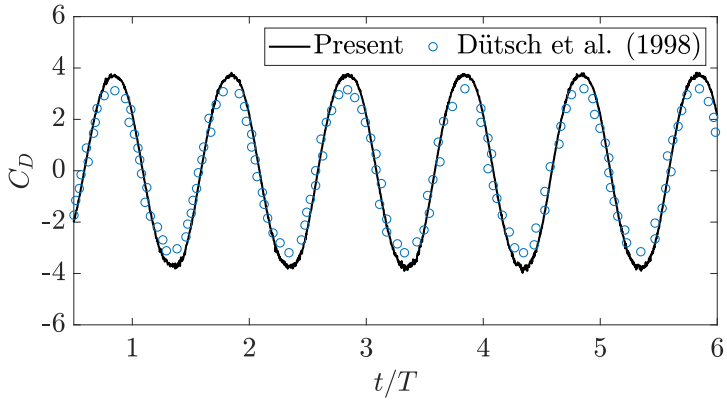

Figure B1. Computed time history of instantaneous drag coefficient C_D of the inline oscillating cylinder in comparison with the result of Dütsch et al. (1998).

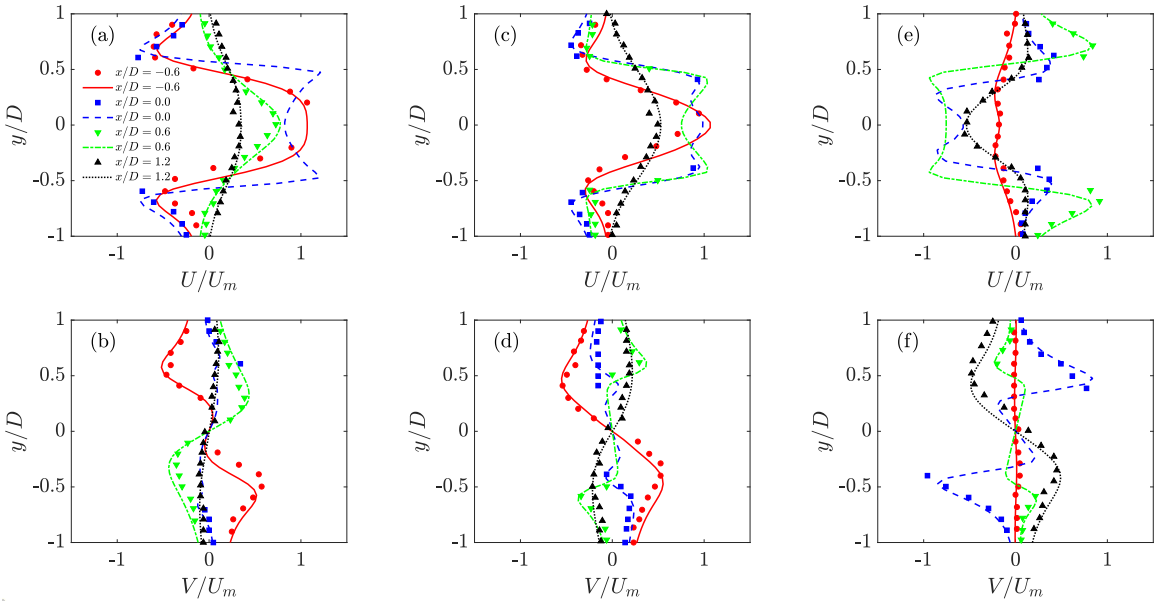

Figure B2. Comparison of velocity components by the present computation (lines) with the experimental data of Dütsch et al. (1998) (symbols) at four cross-sections and three different phase angles: (a, b) $\phi = 180°$; (c, d) $\phi = 210°$; (e, f) $\phi = 330°$. U and V are velocity components in x and y directions respectively.

agreement has been obtained which is also similar to other computational studies (Liao et al., 2010; Li et al., 2016).

Appendix C. Effect of the domain extent

Here we study the effect of the domain extent on the vortex shedding and far-field wake characteristics. The normal streamwise domain length is $L_x = 100c$ (see figure 2), and we extend it to $L_x = 150c$ ($-25 \leq x/c \leq 125$) as the long domain case. Figure C1

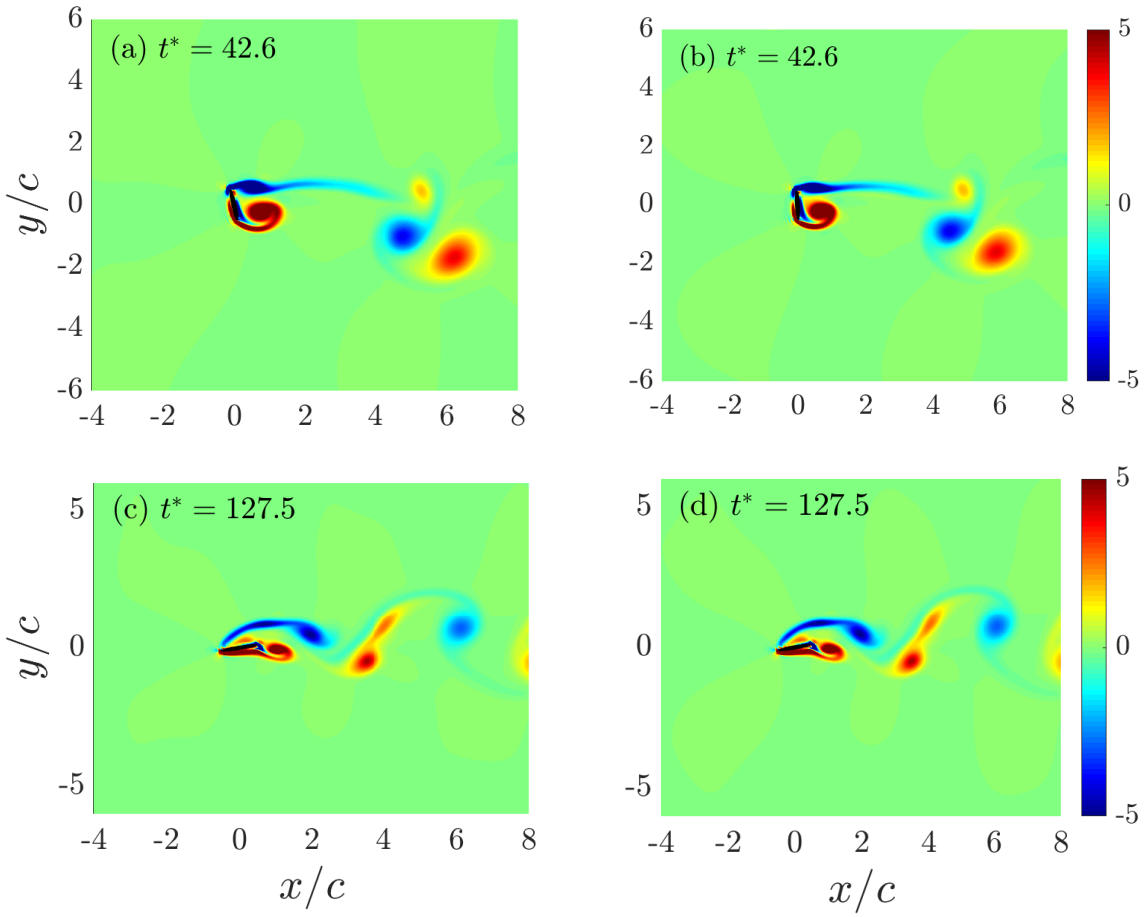

Figure C1. Effect of domain extent on near-foil vortex shedding characteristics ($Re = 200$): (a,b) $\omega^* = 0.20$; (c,d) $\omega^* = 0.60$; (a,c) normal domain; (b,d) long domain.

displays typical near-foil vortical fields of the foil rotating at $\omega^* = 0.20$ and 0.60 with the normal and long domain configurations. And figure C2 shows the corresponding far-field vortical wakes. It is clearly seen that the flow fields computed with the two domains are in excellent coincidence. Therefore, as the normal domain is already long enough, little effect could be introduced by increasing the domain extent.

On the other hand, there seems to exist some kind of vorticity accumulation at the outflow boundary, see figure C2 (a). It is a well-known defect of the Neumann or convective boundary condition at the outflow boundary in the computational methods for incompressible flow around objects (Sani and Gresho, 1994). In the literature, there have been several approaches to relieve the problem (Papanastasiou et al., 1992; Hasan et al., 2005; Dong et al., 2014; Ni et al., 2019), to name just a few. These methodologies could help to significantly reduce the domain extent in the simulation, whereas enough long domain has been adopted in this study and hence implementation of improved

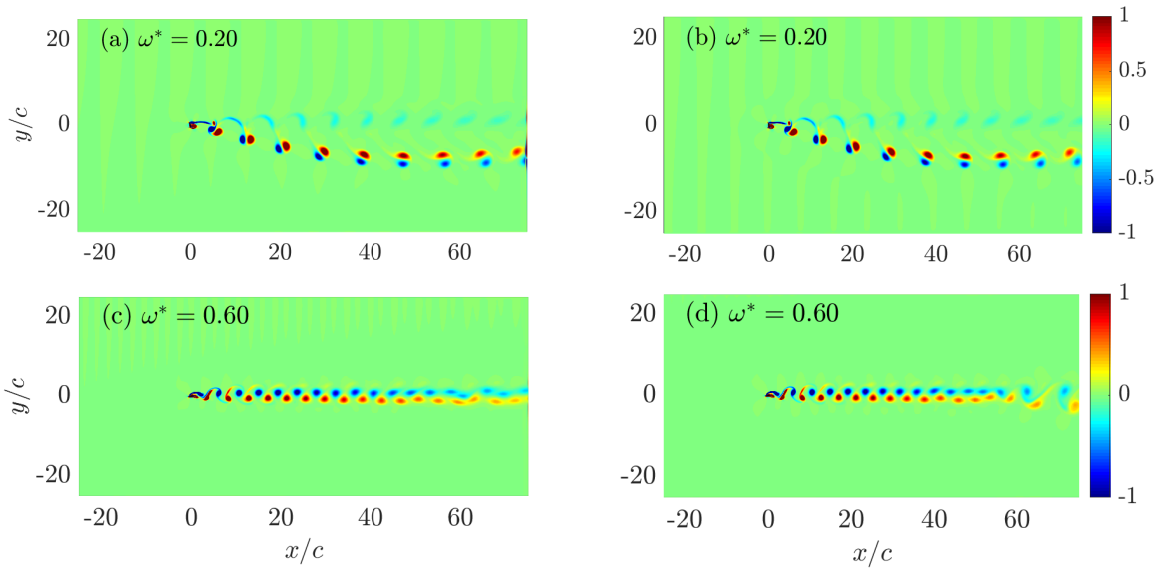

Figure C2. Effect of domain extent on far-field wakes ($Re = 200$): (a,b) $\omega^* = 0.20$; (c,d) $\omega^* = 0.60$; (a,c) normal domain; (b,d) long domain.

outflow boundary condition is reasonably not needed.

References

Akwa J V, Vielmo H A and Petry A P 2012 *Renew. Sustainable Energy Rev.* **16**(5), 3054–3064.

Andersen A, Pesavento U and Wang Z J 2005 *J. Fluid Mech.* **541**, 65–90.

Belmonte A, Eisenberg H and Moses E 1998 *Phys. Rev. Lett.* **81**, 345–348.

Best J L 1998 *Int. J. Multiph. Flow* **24**(5), 693–720.

Breugem W P 2012 *J. Comput. Phys.* **231**(13), 4469–4498.

Chakraborty P, Balanchandar S and Adrian R J 2005 *J. Fluid Mech.* **535**, 189–214.

Domenge P X C, Velez C A and Das T 2016 *Appl. Math. Model.* **40**(13), 6576–6587.

Dong S, Karniadakis G E and Chryssostomidis C 2014 *J. Comput. Phys.* **261**, 83–105.

Dütsch H, Durst F, Becker S and Lienhart H 1998 *J. Fluid Mech.* **360**, 249–271.

Giacobello M, Ooi A and Balachandar S 2009 *J. Fluid Mech.* **621**, 103–130.

Godoy-Diana R, Aider J L and Wesfreid J E 2008 *Phys. Rev. E* **77**, 016308.

Godoy-Diana R, Marais C, Aider J L and Wesfreid J E 2009 *J. Fluid Mech.* **622**, 23–32.

Govardhan R and Williamson C H K 2000 *J. Fluid Mech.* **420**, 85–130.

Graftieaux L, Michard M and Grosjean N 2001 *Exp. Fluids* **12**, 1422–1429.

Greenwell D I and Garcia M T 2014 *J. Fluids Struct.* **49**(8), 640–653.

Hargreaves D, Kakimpa B and Owen J 2014 *J. Fluids Struct.* **46**, 111–133.

Hasan N, Anwer S F and Sanghi S 2005 *J. Comput. Phys.* **206**(2), 661–683.

Heathcote S and Gursul I 2007 *Phys. Fluids* **19**, 027104.

Hu R 2015 *Fluid Dyn. Res.* **47**, 045503.

Hu R and Wang L 2014 *Phys. Rev. E* **90**, 013020.

Hu R, Wang L, Wang P, Wang Y and Zheng X 2018 *Computation* **6**(2), 31.

Hunt J, Wray A and Moin P 1988 *in* 'Proceeding of the Summer Program in Center for Turbulence Research'.

Iversen J D 1979 *J. Fluid Mech.* **92**, 327–348.

Jones K D, Dohring C M and Platzer M F 1998 *AIAA J.* **36**(7), 1240–1246.

Kakimpa B, Hargreaves D and Owen J 2012 *J. Wind Eng. Ind. Aerodyn.* **111**, 104–116.

Kang S, Choi H and Lee S 1999 *Phys. Fluids* **11**(11), 3312–3321.

Kempe T and Fröhlich J 2012 *J. Comput. Phys.* **231**(9), 3663–3684.

Kim J, Kim D and Choi H 2001 *J. Comput. Phys.* **171**(1), 132–150.

Lau E M, Huang W X and Xu C X 2018 *J. Fluid Mech.* **850**, 1009–1031.

Li R Y, Xie C M, Huang W X and Xu C X 2016 *Comput. Fluids* **140**, 122–135.

Liao C C, Chang Y W, Lin C A and McDonough J 2010 *Comput. Fluids* **39**(1), 152–167.

Lin N, Letchford C and Holmes J 2006 *J. Wind Eng. Ind. Aerodyn.* **94**(2), 51–76.

Lu H, Lua K B and Lim T T 2018 *Eur. J. Mech. B-Fluids* **72**, 676–690.

Lua K B, Lim T T and Yeo K S 2010 *Exp. Fluids* **49**, 1065–1084.

Lua K B, Lu H and Lim T 2018 *J. Fluids Struct.* **78**, 36–51.

Lugt H J 1980 *J. Fluid Mech.* **99**(4), 817–840.

Lugt H J 1983 *Annu. Rev. Fluid Mech.* **15**, 123–147.

Lugt H J and Ohring S 1977 *J. Fluid Mech.* **79**, 127–156.

Mittal R, Seshadri V and Udaykumar H S 2004 *Theoret. Comput. Fluid Dyn.* **17**, 165–170.

Naik S N, Vengadesan S and Prakash K A 2017 *J. Fluids Struct.* **68**, 15–31.

Ni N, Yang Z and Dong S 2019 *J. Comput. Phys.* **391**, 179–215.

Papanastasiou T C, Malamataris N and Ellwood K 1992 *Int. J. Numer. Meth. Fluids* **14**, 587–608.

Poon E K W, Ooi A S H, Giacobello M, Iaccarino G and Chung D 2014 *J. Fluid Mech.* **759**, 751–781.

Rao A, Radi A, Leontini J S, Thompson M C, Sheridan J and Hourigan K 2015 *J. Fluids Struct.* **53**, 2–14.

Roy S and Saha U K 2013 *Renew. Sustainable Energy Rev.* **24**(10), 73–83.

Ryu S and Iaccarino G 2017 *J. Fluid Mech.* **813**, 482–507.

Sani R L and Gresho P M 1994 *Int. J. Numer. Meth. Fluids* **18**(10), 983–1008.

Schram C, Rambaud P and Riethmuller M L 2004 *Exp. Fluids* **36**(2), 233–245.

Simpson C E, Babinsky H, Harvey J K and Corkery S 2018 *Exp. Fluids* **59**(125).

Skews B W 1990 *J. Fluid Mech.* **217**, 33–40.

Smith E H 1971 *J. Fluid Mech.* **50**, 513–534.

Stojković D, Breuer M and Durst F 2002 *Phys. Fluids* **14**(9), 3160–3178.

Tachikawa M 1983 *J. Wind Eng. Ind. Aerodyn.* **14**(1), 443–453.

Tam D, Bush J W M, Robitaille M and Kudrolli A 2010 *Phys. Rev. Lett.* **104**, 184504.

Thompson M C, Radi A, Rao A, Sheridan J and Hourigan K 2014 *J. Fluid Mech.* **751**, 570–600.

Uchibori K and Tamura T 2019 *J. Fluids Struct.* **89**, 108–122.

Uhlmann M 2005 *J. Comput. Phys.* **209**(2), 448–476.

Varun A V, Balasubramanian K and Sujith R I 2008 *Exp. Fluids* **45**(5), 857–868.

Vollmers H 2001 *Meas. Sci. Tech.* **12**(8), 1199–1207.

Wang L, Hu R, Zhang J and Ma Y 2015 *Math. Probl. Eng.* **2015**(242917).

Wang S, Zhu L, Zhang X and He G 2011 *J. Fluids Eng.-Trans. ASME* **133**(8), 1–12.

Wang W B, Hu R F, Xu S J and Wu Z N 2013 *J. Fluid Mech.* **733**, 650–679.

Williamson C H K and Roshko A 1988 *J. Fluids Struct.* **2**, 355–381.

Yang X L, Zhang X, Li Z L and He G W 2009 *J. Comput. Phys.* **228**(20), 7821–7836.

Zheng Z C and Wei Z 2012 *Phys. Fluids* **24**(10), 103601.

Zhou Q and Fan L S 2014 *J. Comput. Phys.* **268**, 269–301.

Zhu X, He G and Zhang X 2014 *J. Fluid Mech.* **751**, 164–183.